Mixed positive and negative feedback loops drive diverse single-cell gene expression dynamics

Torkel E. Loman[1,2,3*], Christian P. Schwall[1*], Teresa Saez[1], Yujia Liu[1,4], James C. W. Locke[1,#]

[1]Sainsbury Laboratory, University of Cambridge, Bateman Street, Cambridge, CB2 1LR, UK

[2]Computer Science and AI Laboratory (CSAIL), Massachusetts Institute of Technology, Cambridge, US

[3]Mathematical Institute, University of Oxford, Oxford, OX2 6GG, UK

[4]Present address: Department of Biochemistry and Molecular Biology, University of Chicago, Chicago, US

*Contributed equally

[#] *Email*: james.locke@slcu.cam.ac.uk

Abstract

Genetic circuits with only a few components can generate complex gene regulatory dynamics. Here, we combine stochastic modelling and single-cell time-lapse microscopy to reveal the possible dynamics generated by a key gene circuit motif: the mixed positive/negative feedback loop. Our minimal stochastic model of this motif reveals ten distinct classes of dynamic output, including stochastic pulsing, oscillations, and bistability. We systematically map how the circuit's core parameters can be tuned to generate each of the behaviours. Experimental validation in two different mixed feedback circuits in the bacterium *Bacillus subtilis*, σ^B and σ^V, confirms our model's predictive power. Guided by our simulations, we are able to transition between dynamic behaviours by modulating in vivo parameters. Together, these results demonstrate how mixed feedback loops generate diverse single-cell dynamics, improving our understanding of this common biological network motif and informing our efforts to engineer them for synthetic biology applications.

Introduction

Single-cell approaches have revealed that the outputs of gene circuits can be much more heterogeneous and dynamic than previously thought. Even small circuits with a few components can generate a wide range of regulatory dynamics, including bistability (1,2), oscillations (3,4), excitability (5,6), and pulsatile activation (7,8). Stochastic effects due to low molecule numbers often play a key role in generating these, sometimes beneficial, dynamics (9,10). In this study, we systematically explore the dynamic behaviours produced by a key circuit motif, the mixed positive/negative feedback loop, in which a single component both activates and represses its own expression.

Mixed positive/negative feedback loops are a widespread regulatory motif found in processes such as circadian rhythms (11), neural signalling (12), bacterial competence (13), the cell cycle (14), and DNA damage control (15). Mixed feedback architectures have also been proposed as useful regulatory motifs for synthetic biology applications (16). Despite their broad relevance, we lack a general understanding of the range of behaviours these circuits can generate, and how these are influenced by circuit properties.

To address this, we develop a minimal stochastic model of a mixed positive/negative feedback loop (Figure 1A). Stochastic modelling is essential for capturing intrinsic noise from low molecule numbers and extrinsic fluctuations from cellular processes like growth or energy availability (17–19). While prior models have explained behaviours such as excitability in bacterial competence (13,20) or circadian oscillations (21), these efforts typically model circuit-specific topologies and lack general predictive scope. By instead directly modelling effective properties of a mixed feedback circuit, like feedback strength, time delay, noise, and ultrasensitivity, we can predict what behaviours these motifs can generate.

To validate our model predictions, we turn to bacterial alternative sigma factor circuits. Alternative sigma factors direct RNA polymerase to specific downstream targets and control key processes such as stress response, pathogenicity, and chemotaxis (22). The number of alternative sigma factors varies between bacterial species, ranging from 0 (as found in e.g. *Mycoplasma pneumoniae*), to over 63 (as found in *Streptomyces coelicolor*) (23–25). Crucially, many alternative sigma factor circuits share a conserved mixed feedback motif: the sigma factor activates an operon that encodes both itself and an anti-sigma factor that inhibits its function (Figure 1b) (26–28). This simple, well-characterised, structure makes

sigma factor circuits ideal systems for dissecting how mixed feedback architecture shapes dynamic behaviour.

Single-cell time-lapse fluorescence microscopy has revealed diverse, and often stochastic, gene expression dynamics across alternative sigma factor circuits. Using microfluidic devices such as the mother machine (29), studies have uncovered behaviours including heterogeneous activation (σ^V in *B. subtilis (30)*), stochastic pulsing (σ^M, σ^W, σ^X, σ^D, σ^B in *B. subtilis* and RpoS in *E. coli (8,31,32)*), and a single response pulse (σ^B in *B. subtilis (33)*). Here we use σ^V as a model system for heterogeneous activation and σ^B as a model system for pulsatile dynamics (See Supplementary Figures 1**,** 2 for full network details).

Both systems contain mixed feedback architectures. σ^V is activated by lysozyme stress via cleavage of its anti-sigma factor RsiV (34–40), and in turn activates its own operon containing both *sigV* and *rsiV* (Supplementary Figure 1). σ^B is regulated through a partner-switching mechanism involving its anti-sigma factor RsbW and the anti–anti-sigma RsbV (41–45), forming a more complex feedback structure (Supplementary Figure 2). Despite their biological differences, both systems share a core regulatory motif in which a sigma factor promotes expression of both itself and its anti-sigma factor.

In this work, we develop a general stochastic model of a mixed positive/negative feedback loop. The model predicts ten distinct dynamic behaviours, some of which have been previously observed and others newly predicted, and maps how they emerge from variations in a few biologically meaningful parameters. Using genetically rewired σ^V and σ^B circuits in *Bacillus subtilis* (Supplementary Figures 3**,** 4), we experimentally validate the predicted transitions between behaviours. Our work develops general principles of how these behaviours depend on circuit properties, demonstrating how native or engineered systems can be tuned to generate target behaviours.

Results

A general mixed positive/negative feedback loop model can reproduce experimentally observed sigma factor dynamics

To explore the range of dynamics that mixed feedback loop genetic circuits can generate, we developed a minimal stochastic model (Methods, Figure 1a). In this work, we apply it to sigma factor networks, biologically relevant systems that frequently implement mixed feedback loops (Figure 1b). The model is implemented as a stochastic differential equation (SDE) tracking the concentration of a single component (σ), which both activates and represses its own production through a Hill-type regulatory function. The self-repression is subject to a time delay (τ). In the context of sigma factors, this delay can be motivated either by the anti-sigma factor undergoing additional steps before it can interact with the sigma factor (46), or due to the presence of additional feedback mechanisms (47).

The initial formulation of our model depended on 9 parameters. Because our aim was to understand general qualitative behaviours rather than fit specific datasets, we performed nondimensionalisation, reducing the model to six biologically interpretable parameters (Supplementary Notes 2, Supplementary Tables 1, 2). These are: the system's degree of self-activation (S), self-deactivation (D), the time delay in the self-deactivation (τ), base operon activity (v_0), ultrasensitivity (n), and noise amplitude (η). The deterministic version of the model, which excludes the noise parameter η, is given by:

$$\frac{d\sigma(t)}{dt} = v_0 + \frac{(S \cdot \sigma(t))^n}{(S \cdot \sigma(t))^n + (D \cdot \sigma(t-\tau))^n + 1} - \sigma(t)$$

We implemented noise using the chemical Langevin equation (CLE) (48), a well-established method for modelling noise within gene regulatory networks (49). By representing the system as a stochastic differential equation (SDE), the CLE enables fast stochastic simulations when compared to the more exact Gillespie algorithm (50,51) (Supplementary Notes 3). Our results were not specific to our choice of stochastic interpretation, as we verified that simulating noise through the Gillespie algorithm generated equivalent results (Supplementary Notes 3, Supplementary Figures 5, 6).

We implemented the delay, τ, as a distributed delay using the linear chain trick (Supplementary Notes 4.1, Supplementary Figures 7**,** 8) (52,53). This enabled us to model the system as an SDE, rather than as a Stochastic Delay Differential Equation (SDDE), which is advantageous for model simulation and analysis (Methods). For completeness, we also implemented an SDDE version of the model and confirmed it reproduces key results (Supplementary Notes 4.2, Supplementary Figure 9, Supplementary Table 3). Finally, we note that our minimal mixed feedback loop model captures the range of sigma factor

response behaviours reported in the literature, including heterogeneous activation, stochastic pulsing, and single response pulse (Figure 1C) (8,30,33).

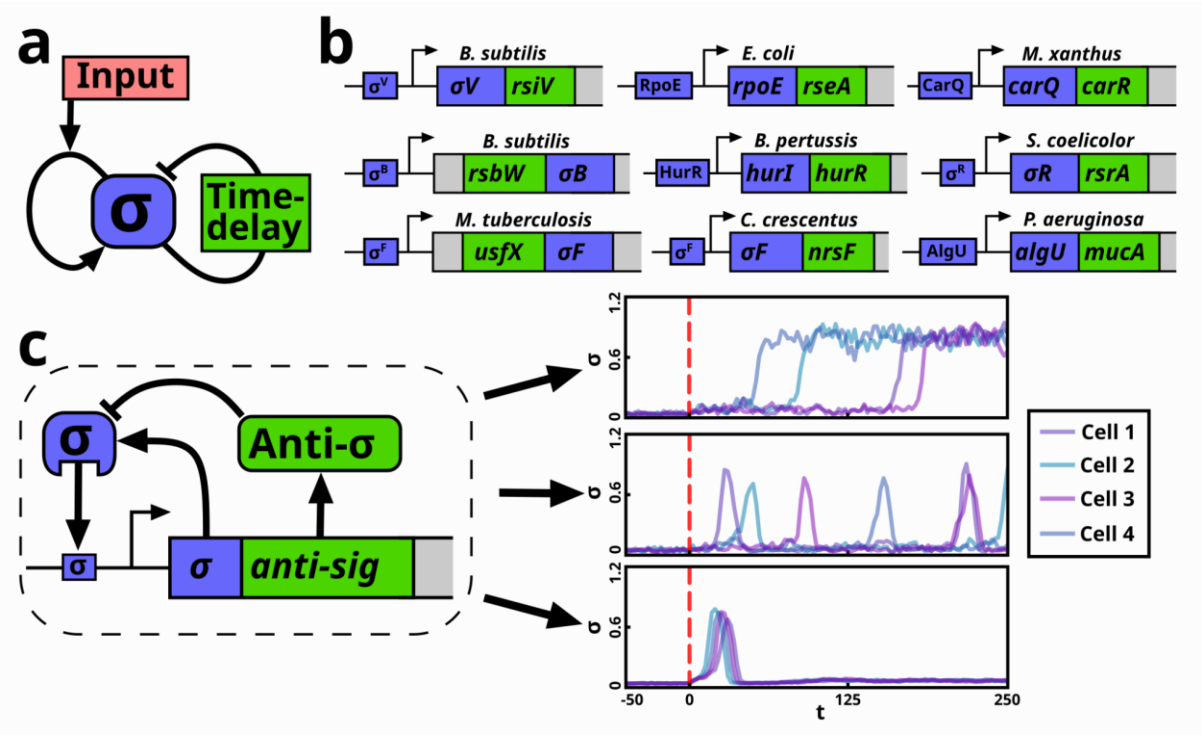

Figure 1: A general model of a mixed positive/negative feedback loop can reproduce experimentally observed sigma factor dynamics. (a) *Schematic of the general mixed positive/negative feedback loop model. Here, a single component (σ) both activates and deactivates its own production. The activation depends on the presence of an input, and the deactivation is subject to a time delay.* ***(b)*** *The mixed positive/negative feedback loop is a common motif among alternative sigma factor circuits. Shown are simplified operon structures of alternative sigma factor circuits in a range of bacterial species, all consisting of a mixed positive/negative feedback. Anti-sigma factors (that repress sigma factor activity) are depicted in green, and sigma factors are depicted in blue.* ***(c)*** *Model simulations can capture known activation behaviours, including heterogeneous activation (top, as observed in e.g. σ^V (30)), stochastic pulsing (middle, as observed in e.g. σ^M (8)), and single pulse dynamics (bottom, as observed in σ^B under environmental stress (33)).*

The model generates ten distinct response behaviours

To explore the range of behaviours the model can exhibit, and to understand how these depend on its parameters, we developed a behaviour classification scheme. The scheme is based on steady state analysis, where we note that the system can have either a fixed point in an inactive state, an active state, both, or a single fixed point of intermediate activity (Supplementary Notes 5, Supplementary Figures 10, 11). Asymptotically, it will approach one of these states. However, perturbations, either due to noise or onset of the input, can cause a transition to another state. By enumerating all possible combinations of these

transitions, we find a total of ten distinct behavioural classes (Figure 2, Supplementary Notes 6, Supplementary Figures 12, 13, 14). By simulating the model across a large set of randomised parameter values and checking that each simulation aligned with one of these ten classes, we confirmed that these classes are robust. (Supplementary Figures 15, 16). Rare additional behaviours that can be considered subclasses of these 10 are discussed in Supplementary Notes 6.4.

Through our classification scheme, we identified ten distinct response behaviours predicted by the model (Figure 2):

1. No activity: The system remains inactive. In the absence of the input, this is also the system's default behaviour (Figure 2a, Supplementary Figure 17).
2. Stochastic pulsing: The system exhibits randomly distributed pulses of activity in time, from an otherwise inactive state (Figure 2b, Supplementary Figure 18).
3. Oscillation: The system alternates between low and high activity in a periodic manner (Figure 2c, Supplementary Figure 19).
4. Stochastic anti-pulsing: The system activates in response to the input, but displays randomly distributed pulses of inactivity over time (Figure 2d, Supplementary Figure 20).
5. Homogeneous activation: In response to the input, the system transitions from an inactive to an active state. The response times are instantaneous (and thus homogeneous across simulations) (Figure 2e, Supplementary Figure 21).
6. Heterogeneous activation: In response to the input, the system transitions from an inactive to an active state. The response times are random (and thus heterogeneous across simulations) (Figure 2f, Supplementary Figure 22).
7. Stochastic switching: The system randomly alternates between an inactive and an active state (Figure 2g, Supplementary Figure 23).
8. Stable bistability: The system has an inactive and an active state, but cannot switch between them intrinsically. An extrinsic way to induce such a switch would be to add additional σ from an external source (Figure 2h, Supplementary Figure 24).
9. Single response pulse: The system exhibits a single pulse of activity at the input's onset, but no significant activity thereafter (Figure 2i, Supplementary Figure 25).
10. Intermediate activation: Following input onset, the system transitions to and remains in a state of intermediate activity (Figure 2j, Supplementary Figure 26). Here, while the activation times are typically homogeneous, certain low-*D* valued regions display heterogeneous intermediate activation (Supplementary Notes 6.4).

These behaviours include all previously observed dynamics among bacterial sigma factors (a single response pulse, stochastic pulsing, heterogeneous activation, and homogeneous

activation) (8,30,31,33), as well as several novel behaviours. Detailed descriptions of each behaviour are provided in the supplementary material (Supplementary Notes 7).

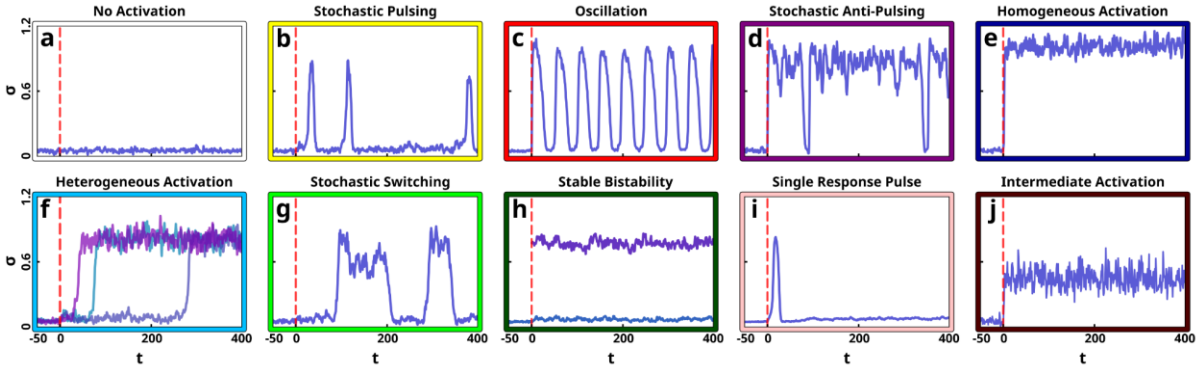

Figure 2. The model generates 10 distinct response behaviours. *Simulations for 10 different parameter sets, demonstrating the 10 different behaviours the model can achieve. Initially, the system remains inactive; upon triggering the input (marked by the red dashed lines), distinct behaviours emerge:* ***(a)*** *No activation.* ***(b)*** *Stochastic pulsing.* ***(c)*** *Oscillation.* ***(d)*** *Stochastic anti-pulsing.* ***(e)*** *Homogeneous activation.* ***(f)*** *Heterogeneous activation (three different simulations displayed).* ***(g)*** *Stochastic switching.* ***(h)*** *Stable bistability. The figure depicts two simulations. The first (dark blue) is initiated at the initial (inactive) state at the same time as the simulations in the other figures. The second (purple) is initiated at the time of the input (dashed red line) in the active state. There is no intrinsic way for the system to switch between these two states (however, it could happen by e.g. the addition of exogenous σ).* ***(i)*** *Single response pulse.* ***(j)*** *Intermediate activation.*

Systematic mapping of behaviours reveals their dependency on model parameters

Next, we investigated how the system's behaviour depends on its six parameters, (S, D, τ, v_0, n, and η). To do this, we developed a heuristic classifier that takes a parameter set as input and assigns it to one of the 10 behavioural classes (Supplementary Notes 8, Supplementary Figure 12). The classifier uses a decision tree in which each node performs simulations initialised at the model's steady states and measures the transition times to other steady states (Supplementary Figure 14). We confirmed the accuracy of the classifier by empirically validating its classifications across a large random sample (Supplementary Figures 15, 16). Applying the classifier across the 6d parameter space allowed us to construct a map showing which behaviour occurs for each parameter combination (Supplementary Notes 8). To visualise how individual system properties influence resulting dynamic behaviours, we plotted 2d slices of this parameter space while holding the remaining four parameters constant (Figure 3).

When examining parameter maps for various values of τ, v_0, n, and η, we found that they can be broadly divided into two regions: $D \lesssim 1$ and $D \gtrsim 1$ (Supplementary Figure 27). Each region is characterised by a distinct behavioural transition as the system's self-activation strength (S) increases. We note that S is a composite parameter which, after non-dimensionalisation, also incorporates the system's input strength. Hence, S can be tuned by either modifying the self-activation strength or by varying the input. In the $D \lesssim 1$ region, the model exhibits behaviours associated with bistability, such as stochastic switching, stable bistability, and heterogeneous activation. Conversely, the $D \gtrsim 1$ region exhibits behaviours related to oscillations and excitability, including stochastic pulsing, oscillations, and stochastic anti-pulsing, although it can also exhibit intermediate activation under some conditions (Supplementary Notes 8, Supplementary Figures 28-32).

Next, we characterised how the behaviours depend on the parameters τ, v_0, n, and η by measuring their effect on the prevalence of each behaviour (Supplementary Figures 17-26). Generally, the time delay τ had the largest effect on system behaviour (after S and D), being especially influential in the $D \gtrsim 1$ region (Supplementary Table 4). Figure 3 illustrates this effect: two maps are shown in which all parameters are held constant except τ, which is 0.2 in the left panel and 5.0 in the right. At low τ, the $D \gtrsim 1$ region supports intermediate activation, while longer delays give rise to stochastic pulsing and oscillations. In contrast, τ has minimal impact in the $D \lesssim 1$ region, where weak self-deactivation renders the delay less consequential. Conversely, v_0 (the base activity of the operon) had only minor effects on the $D \gtrsim 1$ region, while all behaviours in the $D \lesssim 1$ grew less prevalent as v_0 grew larger (Supplementary Notes 7, Supplementary Figure 30, 31). Almost all behaviours were affected by η (the noise amplitude), while n (the degree of system ultrasensitivity) had the least pronounced effect on the system's behaviour (Supplementary Notes 7, Supplementary Figure 29, 31, 32).

Our behaviour maps also permit us to directly observe how noise warps behaviour space. At low noise levels, behavioural transitions coincide well with the bifurcation points of the deterministic system. However, as η (the noise amplitude) is increased, the "effective" bifurcation points, such as those marking the emergence of oscillatory behaviours, increasingly shift in behaviour space (Supplementary Figure 33).

Finally, we note that σ^V and σ^B naturally occupy distinct regions of parameter space, with σ^V exhibiting heterogeneous activation in the $D \lesssim 1$ regime and σ^B showing stochastic pulsing in the $D \gtrsim 1$ regime. This separation allows us to explore different parts of the behavioural map

by selectively tuning parameters in each system. In the following sections, we use σ^V to probe transitions across the *D* axis and σ^B to examine transitions driven by changes in *S*, experimentally validating our model's predictions in both cases.

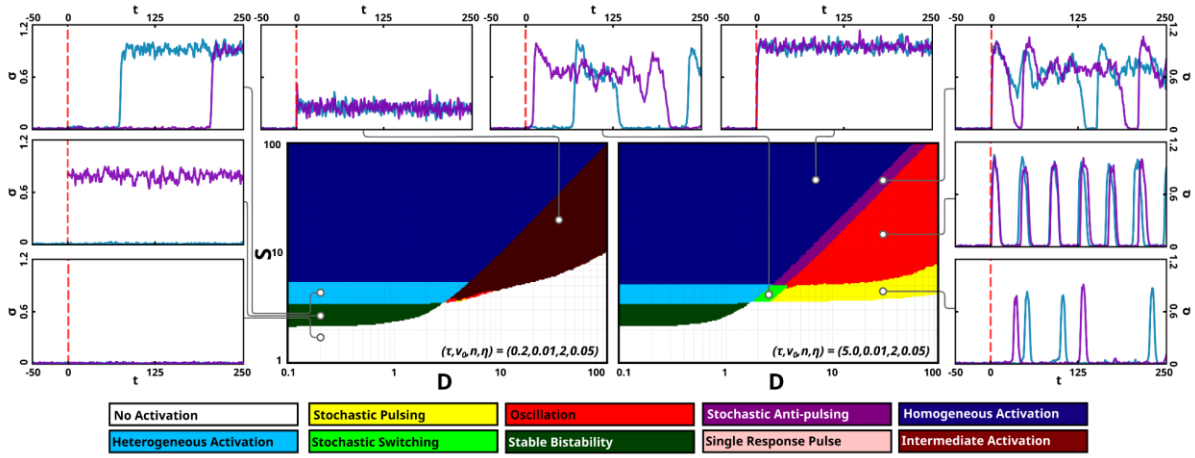

Figure 3. Mapping system behaviours across parameter space reveals distinct dynamic regimes. *We applied our behaviour classifier to each point in 6d parameter space of the model and visualised 2d slices in log-scale S-D space, with the remaining parameters, v_0, n, and η held constant. The two maps shown here differ only in the value of the time delay τ: τ = 0.2 (left) and τ = 5.0 (right). Each point is coloured by the classified dynamic behaviour, and example trajectories from selected points illustrate representative single-cell simulations. While the exact boundaries shift with τ, both maps exhibit a common structure: a D ≲ 1 region with bistable and switching behaviours, and a D ≳ 1 region that supports either intermediate activation (left) or oscillatory and pulsing dynamics (right). In these two maps, the transition occurs at around D ≈ 2, and in general, the transition depends on v_0 but is typically close to 1.This general division by D is robust across parameter choices and is supported by stability analysis (Supplementary Figure 27). The effects of varying τ, v_0, n, and η are further explored in Supplementary Figures 28-32* (which shows additional behaviour maps).

The predicted ability to transition between D≲1 and D≳1 behavioural domains is validated in the σ^V system

We first experimentally tested the transitions predicted for the bistability-dominated *D≲1* region, using the *B. subtilis* alternative sigma factor σ^V as a model system. σ^V regulates the lysozyme stress response in *B. subtilis*, activating genes related to cell wall protection and repair (34,35,37,38,54). In a previous study, we documented the behavioural transition of the wild-type system as *S* is varied (30). In that study, lysozyme stress input was varied, which corresponds to a modulation of *S* in our simulations. Using single-cell time-lapse

289 microscopy, the study demonstrated a transition from no activation, to heterogeneous
290 activation, to more homogeneous activation, as lysozyme was increased, similar to the
291 transitions observed when *S* is increased in the $D \lesssim 1$ region of the parameter map (Figure 3).
292 Although our model often (but not always) includes a stable bistable regime between the no-
293 activation and heterogeneous-activation regions, this behaviour will appear as no activity in
294 these simple input-onset experiments (Supplementary Tables 5, 6). With this consideration,
295 the experimental observations align well with the model predictions.
296
297 Our model predicts that the $D \lesssim 1$ and $D \gtrsim 1$ regions coexists within the same system, and that
298 increasing *D* (the strength of self-deactivation) can shift the system from one regime to the
299 other. To test this, we engineered a series of modified σ^V circuits in which *D* was increased
300 by adding additional copies of the anti-sigma factor (*rsiV*) (Methods) (Supplementary Figure
301 3). As *rsiV* expression is upregulated by σ^V and RsiV inhibits σ^V activity (39,40), this
302 manipulation allows us to tune the system's self-deactivation strength.
303
304 According to our model, increasing *D* should progressively reduce σ^V activity in the ON state
305 while preserving heterogeneous activation; at sufficiently high *D*, all activity should be
306 suppressed (Figure 4a–b, d). We tested these predictions using single-cell microscopy in the
307 mother machine microfluidic device. Six P_{sigV}-*YFP* reporter strains, each containing different
308 copy numbers of *rsiV* (and therefore different *D* levels), were subjected to 1 µg/mL lysozyme
309 stress. As the copy number of *rsiV* increased, the trend of σ^V ON-state activity decreased as
310 expected, while its heterogeneity remained, consistent with the model's predictions. At the
311 highest *D* levels, σ^V activity was entirely suppressed (Figure 4c,e, Supplementary Figures
312 34, 35).
313
314 Finally, we examined the σ^V system's behaviour once it has transitioned into the $D \gtrsim 1$
315 regime. According to our model, this regime supports two possible *S*-transitions depending
316 on the values of the remaining parameters τ, v_0, n, and η, with τ having the primary effect
317 (Supplementary Notes 8). These transitions include either pulsing/oscillatory behaviours, or
318 intermediate activation (Figure 3, Supplementary Figures *28-32*).
319
320 To identify in which region of parameter space the system is in, we modulated *S* in our two
321 high *D* strains by adding an additional copy of *sigV* driven by its own promoter and by
322 varying lysozyme stress levels. We found that σ^V's transition specifically falls into the
323 intermediate activation category (Figure 4f-h). Our model predicts that the intermediate
324 activation behaviour's steady state activity is smoothly tuned by the levels of *S* and *D,* with *S*
325 increasing activity whilst D reduces it (Figure 4i). We confirmed this experimentally (Figure

4j, Supplementary Movie 1). We also note that activation times are homogeneous in both simulation and experiment, further suggesting that the system has transitioned out of the heterogeneous activation domain observed for lower *D* values (Figures 4k-l). Together, these results confirm our prediction that, by tuning system parameters, a mixed feedback loop can transition between dynamically distinct behavioural regions.

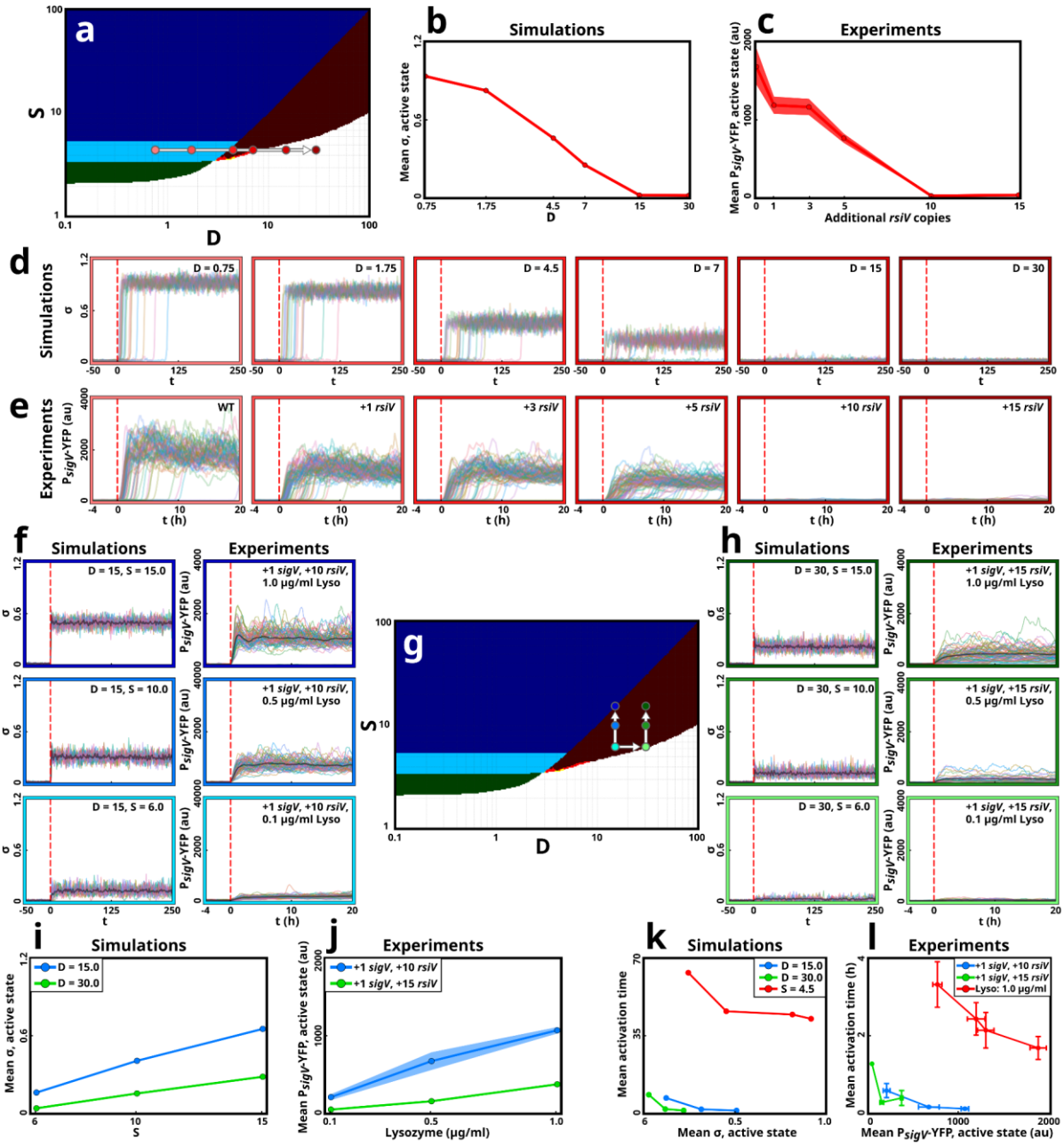

Figure 4. The model's predicted transition between the heterogeneous and intermediate activation behavioural domains are validated in the σ^V system. The model predicts that, as *D* is increased, *σ*'s steady state activity is reduced while its heterogeneous activation remains. For high enough *D* levels, the system is fully inactivated. Here, it exhibits an intermediate activation transition as *S* is varied (unlike the heterogeneous activation transition previously observed for low *D* levels). **(a)** Six representative D values sampled

339 from the model's *S*-*D* behaviour map. **(b)** Simulated ON-state mean *σ* levels for the six
340 points marked in a declines as *D* increases. **(*c*)**. For six different experimental *D* values,
341 mean P_{sigV}-YFP expression after 1 µg/mL lysozyme stress are shown. This confirms the
342 decrease in ON-state activity with increasing *D* as predicted by the model. (**d**) Single-cell
343 simulation traces (*n = 20*) for each condition in **a**. **(e)** Experimental single-cell fluorescence
344 trajectories under 1 µg/mL lysozyme, recapitulating the simulated shift from heterogeneous
345 activation to inactivity. **(f)** For fixed *D = 15*, the model (left) shows an intermediate activation
346 transition as *S* is increased (simulations for *S = 6, 10, 15*). The ON-state activity increases
347 with *S*. Experimental single-cell traces (right) for three lysozyme concentrations (0.1, 0.5, 1
348 µg/mL) validates this transition in a high-*D* σ^V strain (which carries 10 additional *rsiv* and one
349 additional *sigV* copy). **(g)** The six *S*-*D* combinations used in **f** and **h**'s location in parameter
350 space. **(h)** As *D* is increased (to *30*), the model (left) predicts a similar transition as in **f**, but
351 with lower ON-state activity. We replicate this *D* increase by adding 5 *rsiV* copies to the
352 strain used in **f**. Just like the model, this strain (right) replicates the transition in **f**, but with
353 reduced ON-state activity. **(i,j)** Mean ON-state activity levels, as depending on *S*, for the
354 simulations **(i)** and experiments **(j)** shown in **f** and **h**. **(k,l)** In the model **(k)** and experiment **(l)**
355 the intermediate activation transitions (red and green lines) exhibit homogeneous activation,
356 unlike the transition in **a** (red lines) which activates heterogeneously. All experiments have
357 n=3-4 independent repeats.
358

359 The predicted pulsing/oscillatory behavioural transition is
360 validated in the σ^B system

361
362 Next, we experimentally tested the prediction from Figure 3 that increasing *S* can drive the
363 system from stochastic pulsing into sustained oscillations. To do so, we used σ^B, the master
364 regulator of the general stress response in *B. subtilis (55–57)*. Under persistent energy
365 stress, σ^B exhibits stochastic pulsing (8,31). Our parameter maps predict a range of
366 behaviours that can be generated from stochastic pulsing, such as oscillations, by tuning
367 the value of *S*.
368
369 Normally, observation of potential high-*S* behaviours (such as oscillations) by tuning energy
370 stress levels is not possible in σ^B, as high energy stress causes secondary effects such as
371 cell death. To avoid this issue, we rewired the σ^B circuit to synthetically drive σ^B via its
372 energy stress pathway, adapting an approach previously used to re-wire σ^B via the
373 environmental stress pathway (31). In a *B. subtilis* strain containing a reporter for σ^B activity,
374 P_{sigB}-*YFP*, we first knocked out *rsbP* and *rsbU*, the upstream phosphatases that activate the
375 anti-anti-sigma factor RsbV under stress (Methods). Next, we chromosomally integrated a
376 mutated form of RsbP, which is constitutively active, under the control of an IPTG inducible
377 promoter to drive σ^B expression (Supplementary Figure 4). The mutated RsbP had the PAS

378 and coiled-coil region removed causing it to be constitutively active (58).This enabled us to
379 experimentally vary *S* by adding IPTG to the growth medium, allowing us to investigate the
380 system's response across a range of values.
381
382 We scanned our parameter space maps to determine which transition the system
383 undergoes, given it starts in stochastic pulsing (the behaviour found in σ^B), as *S* is
384 modulated (Supplementary Notes 8). We note that stochastic pulsing is almost exclusively
385 preceded (for lower *S*) by no activation, and proceeded (for higher *S*) by oscillation
386 (Supplementary Tables 5). In addition, for high enough *S*, the system activates
387 homogeneously. Finally, for some systems, the oscillating and the homogeneous activation
388 regions are separated by a region of stochastic anti-pulsing (Figure 5a, Supplementary
389 Tables 5, 6, Figures *28-32*).
390
391 Next, we measured the σ^B activity of our rewired P_{sigB}-*YFP* strain in the mother machine
392 microfluidics device across various concentrations of IPTG (Methods). As IPTG levels
393 increased from low to high, the σ^B system transitioned through no activation, stochastic
394 pulsing, oscillation, and homogeneous activation behaviours, similar to as predicted by the
395 model (Figure 5b, c, Supplementary Figures 36-39, Supplementary Movie 2). To further
396 validate these findings, we developed a new classifier capable of quantifying these four
397 behaviours' occurrences in both model simulations and experimental time trajectories. Unlike
398 the original classifier, which relies on analytical steady-state analysis of parameter values
399 and cannot be applied to experimental data, this new classifier works directly with time-
400 series data (Supplementary Notes 11, Supplementary Figures 40, 41). Applying it to both
401 model and experimental data revealed that they undergo the same transition (Figure 5d).
402
403 We note that the stochastic anti-pulsing behaviour predicted by the model is not reproduced
404 experimentally. This discrepancy could be explained by the half-life of the fluorescent marker
405 for σ^B not providing high enough time resolution to distinguish the anti-pulses, or by
406 additional complexity of the σ^B pathway enabling a different transition than what is predicted
407 by our minimal model. Furthermore, the stochastic anti-pulsing behaviour only occurs for
408 some combinations of τ, v_0, n and η, while for others, oscillation transitions directly to
409 homogeneous activation. While the former transition is about six times more common, we
410 cannot here confirm which one σ^B exhibits (Supplementary Tables 5, 6, Figures *28-32*).
411 Notably, the transition from stochastic pulsing to oscillations and then to homogeneous
412 activation, as predicted by our minimal model and supported by experimental observations,
413 also matches the transition identified in a previous stochastic model of the full σ^B circuit (59).

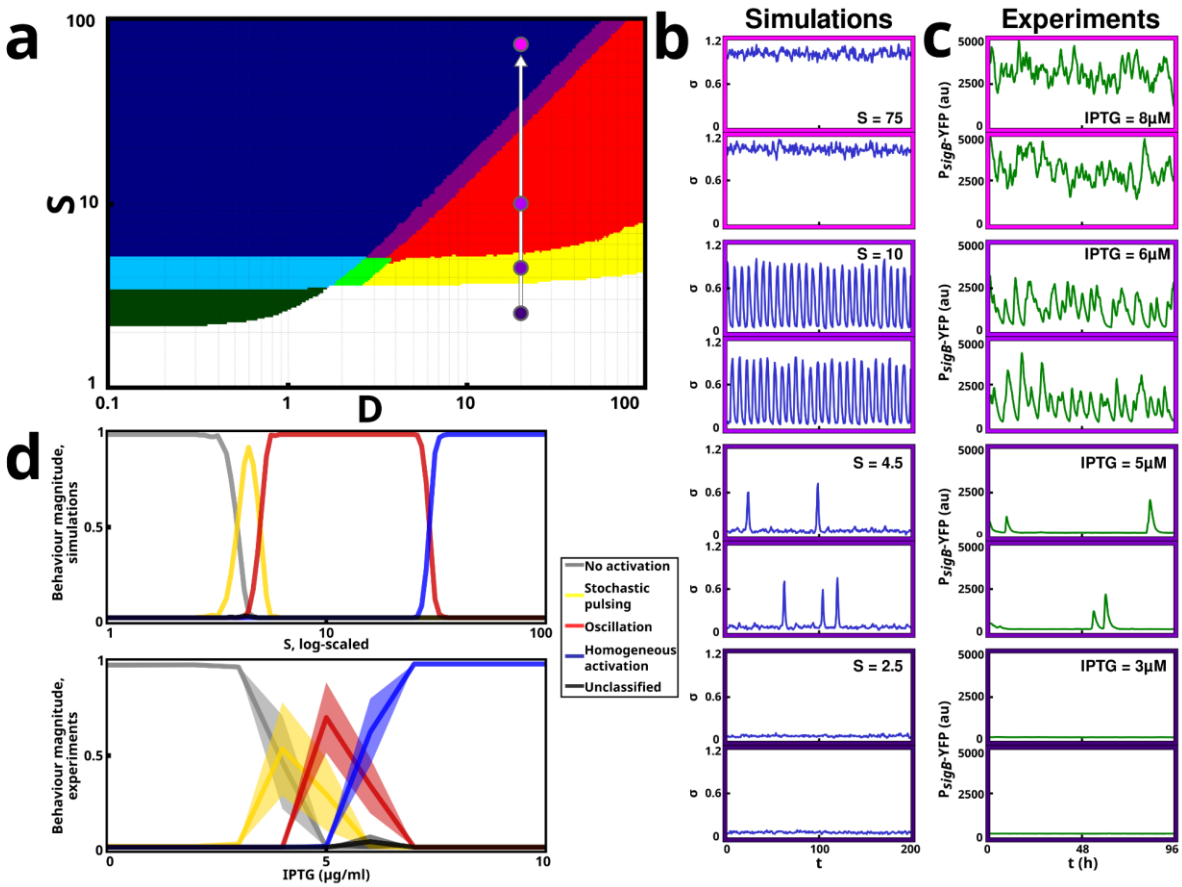

Figure 5. The model's predicted transition through the pulsing/oscillatory region is validated in the σ^B system. (a) *A behaviour map in which increasing self-activation strength (S) in the D ≳ 1 region drives a transition from stochastic pulsing to oscillations.* ***(b)*** *Simulated trajectories at four different S values (purple dots in* ***a****) under constant input, illustrating the predicted progression through no activation, stochastic pulsing, oscillations, and homogeneous activation.* ***(c)*** *Representative single-cell traces of the rewired B. subtilis* P_{sigB}*-YFP strain (Methods) at increasing IPTG concentrations, showing the same behavioural sequence as in the model.* ***(d)*** *A classifier applicable to both simulation and experiment was developed to assign time-trajectories to one of four classes: no activation, stochastic pulsing, oscillation, or homogeneous activation (Supplementary Notes 11). Applied to simulated (from the parameter slice in* ***a****) and experimental (2–9 μg/mL IPTG) trajectories, the classifier confirms that both systems exhibit the same transition sequence. Shaded regions show standard deviation over n = 3-5 experimental replicates.* The "unclassified" behaviour (black) indicates the (very few) trajectories the classifier failed to assign to either one class.

Discussion

In this work, we present a general model of a mixed positive/negative feedback loop, which defines ten distinct dynamic behaviours this motif can generate (Figure 2). By employing an automated classification scheme, we mapped the occurrence of these behaviours across parameter space, revealing how each behaviour depends on the system's properties (parameters) (Figure 3). To demonstrate our model's applicability to real systems, we apply its predictions to bacterial sigma factors, a group of commonly studied systems whose circuits contain mixed positive/negative feedback loops.

We divide parameter space into two approximate regions, $D \lesssim 1$ and $D \gtrsim 1$, each undergoing a distinct behavioural transition as the input (or self-activation) parameter, S, is varied (Supplementary Figure 27). For $D \lesssim 1$ the transition is characterised by bistable behaviours, while for $D \gtrsim 1$ a range of pulsing and oscillatory behaviours are exhibited. To validate our model, we examined the behaviours of two real systems (the alternative sigma factors σ^V and σ^B, both from *B. subtilis*) as S is increased from small to large. Here, both systems undergo the predicted transition (Figures 4, 5). Furthermore, we showed that by increasing the value of D, a system in the $D \lesssim 1$ region (e.g σ^V) can be induced to produce $D \gtrsim 1$-type behaviours. This shows that these two regions, as predicted by the model, can coexist in the same system (Figure 4).

The mixed positive/negative feedback loop is a common motif in cellular pathways. Our work provides a comprehensive understanding of how these systems generate a wide range of behaviours. A detailed analysis of each behaviour and their dynamics is provided in Supplementary Notes 7. Specifically for bacterial sigma factors, several behaviours predicted by our model, including single response pulse, stochastic pulsing, and heterogeneous activation, have been observed using single-cell microscopy (30,32,33,60). We demonstrate that these behaviours can be explained by the core mixed positive/negative feedback loop inherent in these systems (Figure 1c). Crucially, our model enables both forward and inverse predictions: it can predict which behaviours a circuit will exhibit given its properties, and conversely, infer likely circuit properties from observed behaviours. For example, the σ^B circuit, which displays stochastic pulsing, is predicted to operate at a higher self-deactivation strength (D) than the σ^V circuit, which displays heterogeneous activation. As more sigma factor systems are explored, our model predicts that additional predicted behaviours may also be observed. Beyond sigma factors, our findings may generalise to

mixed feedback loops in other biological and non-biological systems, including electronic control circuits, ecological models, and neural networks (12,61–63).

A central advantage of our approach is the use of a minimal, coarse-grained model to capture the essential dynamics of gene regulatory circuits. By not reproducing the detailed biochemistry of specific systems, our model allows us to make conclusions that can be generalised across mixed feedback loops. Furthermore, by testing these predictions *in vivo*, we confirm that our analysis holds when applied to real systems containing additional complexity, supporting the use of minimal models to make biologically relevant predictions. Finally, we show that noise not only enables qualitatively distinct dynamic behaviours, such as stochastic pulsing and heterogeneous activation, but also causes non-intuitive shifts of the boundaries between behavioural regimes in parameter space, effectively ‘warping’ the behavioural boundaries (Supplementary Figure 33).

Our insights are also relevant to synthetic biology, where mixed positive/negative feedback loops, such as those involving sigma factor circuits, have been proposed as potential regulators of synthetic systems (64–66). Here, we have only experimentally tuned two of the six parameters (S and D). Furthermore, the large number of additional genes required to tune D limits the practicality of our approach for most applications. In the future, it will be important to explore whether synthetic mixed positive/negative feedback loops that allow for tuning additional properties can be developed. Here, our work provides a blueprint for predicting and engineering circuit behaviours from minimal models, offering a foundation for designing synthetic regulators with tailored dynamic responses.

Materials and Methods

Mathematical model

Our minimal model of a general mixed positive/negative feedback loop tracks the concentration of a single component (σ). Degradation/dilution was assumed to be linear. To make production as general as possible, it was modelled as a Hill function. The model is based on the following three assumptions:

- σ activates its own production.
- σ deactivates its own production.

- The deactivation is subject to a time delay.

To take these into account, production depended on both an activating term (σ) and a repressing term (σ subject to a time delay).

The time delay was implemented using the linear chain trick (LCT) (52,53). While this introduces additional variables to the system, it has the advantage that the model can be represented as ODEs and SDEs (instead of DDEs and SDDEs). After confirming that the number of intermediaries used in the LCT had little effect on the model, we decided to implement it using three intermediaries (Supplementary Figures 7, 8, Supplementary Notes 4.1). Finally, we also confirmed that all ten response behaviours could be recreated in a model with a discrete delay (Supplementary Figure 9, Supplementary Notes 4.2).

Initially, our model depended on 9 parameters. Since we only sought to investigate qualitative behaviours, nondimensionalisation was performed. This section will describe the nondimensionalised model. The nondimensionalisation process and the non-nondimensionalised model are described in Supplementary Notes 2.

Reactions

Initially, our model contains only two reactions, production and degradation (or dilution) of the sigma factor (σ, the model's only species). An additional three production and degradation reactions are added by the LCT (which also adds three intermediary species, A_1, A_2, and A_3). These reactions are described in Table 1.

Description	Reaction	Rate	Propensity
Production	$\emptyset \longrightarrow \sigma$	$V_0 + (S[\sigma])^n/((S[\sigma])^n+(D[A_3])^n+1)$	$V_0 + (S[\sigma])^n/((S[\sigma])^n+(D[A_3])^n+1)$
Degradation/dilution	$\sigma \longrightarrow \emptyset$	1	$[\sigma]$
Production (LCT)	$\emptyset \longrightarrow A_1$	$[\sigma]/\tau$	$[\sigma]/\tau$
	$\emptyset \longrightarrow A_2$	$[A_1]/\tau$	$[A_1]/\tau$
	$\emptyset \longrightarrow A_3$	$[A_2]/\tau$	$[A_2]/\tau$
Degradation/dilution	$A_1 \longrightarrow \emptyset$	$1/\tau$	$[A_1]/\tau$

(LCT)	A_2 —> ∅	1/τ	$[A_2]/\tau$
	A_3 —> ∅	1/τ	$[A_3]/\tau$

Table 1: *The reactions of the general sigma factor circuit model. The model primarily consists of two reactions, production and degradation of the sigma factor (σ). However, since the time delay (of the negative feedback of σ on its own production) is implemented using the LCT, an additional 3 species (*A_1, A_2, and A_3*) are introduced. This also adds an additional three production and three degradation reactions.*

Parameters

Our nondimensionalised model consists of 6 parameters, as described in Table 2. The model does not have specific parameter values. Instead, every instance of the model, with specific values of (S,D,τ,v_0,n,η) represents a potential mixed positive/negative feedback loop. E.g. by letting S be large and D small, we can investigate the behaviour of circuits with high degrees of self-activation and low degrees of self-deactivation. As we scan these parameters' values we can investigate how systems' properties affect their behaviours. These scans are made possible through the nondimensionalisation process, which reduces the dimension of parameter space.

Parameter	Description
S	Degree of self-activation (also includes input strength).
D	Degree of self-deactivation.
τ	Length of the self-deactivation time delay.
v_0	Operon base activity/leakage.
n	Hill coefficient (degree of non-linearity in the circuit).
η	Degree of noise in the circuit.

Table 2: *The parameters of the (non-dimensionalised) general sigma factor model.*

We note that the parameter S is a composite of the pre-nondimensionalised parameters $\hat{S}$ and $\hat{I}$, where $\hat{S}$ is the degree of system self-activation, and $\hat{I}$ the magnitude of the input signal (Supplementary Notes 2). Hence, modulation of a system's input corresponds to modulation of the parameter S.

Model Simulations

We wish to investigate the model's behaviour in response to an input. In the absence of the input (in response to which we wish to investigate the response), $S=0$. When we simulate our model for a specific parameter set (S,D,τ,v_0,n,η), we will initialise it with $S=0$, with the parameter S only attaining its designated value at the time of input onset (always at time $t=0$). E.g. a model instance may be defined by the parameter set $(S,D,\tau,v_0,n,\eta)=(5.0,5.0,10.0,0.1,2,0.1)$, and simulated throughout the time interval $(-500,2000)$. The simulations start with the parameter values $(0.0,5.0,10.0,0.1,2,0.1)$, which are changed to $(5.0,5.0,10.0,0.1,2,0.1)$ at time 0, at which point the system activates.

It would be possible to vary the value of S throughout a simulation, to model inputs with varying magnitude. However, for simplicity, this work will only consider systems with a step increase in the input.

Practically, the model was implemented using in the Julia programming language using the Catalyst.jl modelling package (67). All simulations were carried out using the DifferentialEquations.jl package (68). The ImplicitEM solver was used as it handles stiff SDE systems well, and allows for adaptive time stepping (69). Stochastic chemical kinetics were simulated using Gillespie's direct algorithm using the JumpProcesses.jl package (70).

Automated behaviour classification

Initial steady state and stability analysis of our model determined that it may have either 0, 1, or 2 stable steady states (Supplementary Notes 5). While a dynamic system asymptotically approaches a stable steady state, perturbations may cause a transition towards another steady state. Such perturbations may either be transient (change in input magnitude) or asymptotic (noise). Based on the possible transitions between the system's potential steady states, we designed a classification scheme for the system's behaviour (Supplementary Notes 8). This scheme takes into account the possibility of excitable and oscillatory behaviours. A total of 10 system behaviours (as described in the Results) were predicted. Further behaviours could be created by subdividing the initial ten, however, we deemed such subdivisions non-beneficial (Supplementary Notes 6.4). Further description and analysis of the individual behaviours can be found in Supplementary Notes 7.

To enable our mapping of behaviour across parameter space, we created a decision tree-based heuristic classifier algorithm. When provided a parameter set (S,D,τ,v_0,n,η), the

algorithm simulates the model multiple times, and assigns it one of the behavioural classes described in Figure 2. The full algorithm is described in Supplementary Notes 8. In addition, to further prove its validity, we randomly generated 10 parameter sets from each behaviour (as classified by the algorithm). By showing that simulations of these parameter sets align with their designated behaviours, we demonstrate the efficacy of the algorithm (Supplementary Figures 15, 16).

Bifurcation analysis

Bifurcation diagrams were generated using the BifurcationKit.jl software (71).

Experiments

Strains and Media

All strains are derived from *B. subtilis* 168 or PY79. Deletions were made by recombination of linear DNA fragments homologous to the region of interest and replacing the gene of interest with an antibiotic resistance cassette. All strains had a housekeeping σ^A promoter-driven mCherry as a constitutive control and for segmentation.

Cells were grown in Spizizen's Minimal Media (SMM) (72). It contained 50 µg/ml Tryptophan as an amino acid source and 0.5% glucose as a carbon source. Cultures were started from frozen stock in SMM and grown overnight at 30°C to an OD between 0.3 and 0.8. The overnight cultures were resuspended to an OD of 0.01 and regrown to an OD of 0.1 at 37°C.

Plasmids

E. coli strain DH5α was used to clone all plasmids. The cloning was done with a combination of standard molecular cloning techniques using Clonetech In-Fusion Advantage PCR Cloning kits and non-ligase dependent cloning. Plasmids were chromosomally integrated into the 168 or PY79 background via double crossover using standard techniques. The list below provides a description of the used plasmids, with details on selection marker and integration position/cassette given at the beginning. Note that all plasmids below replicate in *E. coli* but not in *B. subtilis.*

.

1. **ppsB::P$_{trpE}$ - *mCherry* ErmR**

   This plasmid was used to provide uniform expression of mCherry from a σ^A-dependent promoter, enabling automatic image segmentation (cell identification) in time-lapse movie analysis. A minimal σ^A promoter from the *trpE* gene was cloned into

612 a vector with *ppsB* homology regions (31). The original integration vector was a gift
613 from A. Eldar (73).
614
615 **2. sacA::P$_{sigB}$-*YFP* CmR**
616 The target promoter of *sigB* was cloned into the EcoRI/BamHI sites of AEC127 (73)
617 yielding a Venus (YFP) reporter for σ^B activity (gift from M. Elowitz, CalTech).
618
619 **3. amyE::P$_{hyperspank}$-*rsbP*Δ4 (ΔPAS-CC)**
620 The coding region of a *rsbP* mutant lacking PAS and the coiled-coil region along with
621 a 5' transcriptional terminator, was cloned downstream of the hyperspank IPTG-
622 inducible promoter in plasmid pDR-111 (gift from D. Rudner, Harvard). *rsbP*Δ4
623 (ΔPAS-CC) is described in (58).
624
625 **4. *sacA*::P$_{sigV}$-*YFP* CmR**
626 The target promoter of *sigV* was cloned into the EcoRI/BamHI sites of AEC12 (Eldar
627 *et al,* 2009) (gift from M. Elowitz, CalTech).
628
629 **5. *amyE*::P$_{sigV}$-? x *rsiV* SpecR**
630 The target promoter of *sigV* with multiple copies of *rsiV* (?= 1x, 3x, 5 x) were cloned
631 into the sites EcoRI/BAmHI and BamHI/HindIII of pdL30 (Locke et al, 2011).
632
633 **6. *lacA*::P$_{sigV}$ - 5 x *rsiV* TetR**
634 The target promoter of *sigV* with five copies of *rsiV* was cloned into the sites
635 EcorI/Nde of a variation of ECE174 (gift from M. Elowitz, CalTech).
636
637 **7. *pyrD*::P$_{sigV}$ - 5 x *rsiV* NatR**
638 The target promoter of *sigV* with five copies of *rsiV* was cloned into the sites
639 EcoRI/BAmHI of a variation of ECE174 (gift from M. Elowitz, CalTech).
640
641 **8. *hag*::P$_{sigV}$-*sigV* ErmR**
642 The target promoter of *sigV* driving *sigV* and 400 upstream and downstream
643 homology regions of hag was cloned into EcorV of pBS II SK
644

645 ## Strain List
646

Strain Name	Genotype	Source
PY79	BGSC 1A747	BGSC
PB2	168 (trpC2)	BGSC
JP1/JLB54	PY79 *ppsb*::P_{trpE} - *mCherry* (Phleo^R)	(8)
JP2	JP1; *ytvA*::*neo*	(8)
JLB047	JP2; *sacA*::P_{sigV}-YFP (Cm^R)	(30)
JLB130	JLB047; *hag*::ErmR	(30)
JLB212	JLB130; *amyE*::P_{sigV}-*rsiV* SpecR	(30)
JLB288	JLB130; *amyE*::3x P_{sigV}-*rsiV* SpecR	This work
JLB293	JLB130; *amyE*::5x P_{sigV}-*rsiV* SpecR	This work
JLB325	JLB293; *lacA*::5x P_{sigV}-*rsiV* TetR	This work
JLB324	JLB325; *pyrD*::5x P_{sigV}-*rsiV* NatR	This work
JLB327	JLB47; *lacA*::5x P_{sigV}-*rsiV* TetR *amyE*::5x P_{sigV}-*rsiV* SpecR *hag*:: P_{sigV}-*sigV* ErmR	This work
JLB345	JLB47; *amyE*::5x P_{sigV}-*rsiV* SpecR *lacA*::5x P_{sigV}-*rsiV* TetR *pyrD*::5x P_{sigV}-*rsiV* NatR *hag*::P_{sigV}-*sigV* ErmR	This work
JJB176	PB2; *ppsb*::P_{trpE}-*mCherry* Phleo R	(31)
JJB213	JJB176; *sacA*::P_{sigB}-YFP CmR	(31)
JJB240	JJB213; *rsbU*::KanR	(31)
JJB441	JJB240; *amyE*::$P_{hyperspank}$-*rsbP*Δ4 (ΔPAS-CC) SpecR	This work
JLB264	JJB441; *rsbQP*::TetR	This work
JLB346	JLB264; *hag*::ErmR	This work

Table 3: *List of strains used in this article.*

Microscopy

An inverted Nikon Ti-E microscope (Nikon, Netherlands) with a Photometrics Prime sCMOS camera (Photometrics, USA) and a 100x phase Plan Apo (NA 1.4) objective (Nikon, Netherlands) were used for all experiments. Brightfield illumination was provided by a LED

652 lamp (CoolLED, UK) and for Epifluorescence illumination a Lumencore Solar II light engine
653 (Lumencore USA) was used. Chroma filters (Chroma, Bellows Falls, USA) #41027 for the
654 RFP channel and #49003 for the YFP channel were used in combination with the
655 epifluorescence. For temperature control a stage incubator (Solent Scientific, UK) was set at
656 37°C for all experiments. Metamorph (Molecular Device, Sunnyvale, CA, USA) controlled the
657 camera, the motorised stage (Nikon, Amsterdam, Netherlands) and the microscope.

658 Microfluidic Designs

659 Two microfluidic designs were used in this study. All experiments on σ^B were done in a
660 traditional mother machine device (29). The master for these chips was fabricated by
661 exploiting a Kloe Dilase 650, direct laser writer (Kloe, France). More details on the
662 fabrication can be found in the Supplementary Notes 12. All experiments on σ^V were done in
663 a mother machine device with side trenches (74). This epoxy master was a kind gift from the
664 Ellowitz lab.

665 Microfluidic Chip fabrication

666 All microfluidics chips were made using Sylgard 184 polydimethylsiloxane (PDMS) (Dow
667 Corning, USA) using a 10:1 base to curing agent ratio. The PDMS was poured onto the
668 silicon master and cured at 65C for 2h. Chips were cut out and inlets were punched into the
669 PDMS using a 1 mm biopsy puncher (WPI, UK). The chips were then plasma bonded to
670 glass bottom dishes (Wilco Wells, Netherlands) using a Femto Plasma System (Diener,
671 Germany) (12s at 30W and 0.35 mbar). To strengthen the bonding of the PDMS to the glass
672 dish the chips were put into the oven for 10 min at 65°C.

673 Microfluidic Experiments

674 10 ml of the regrown overnight culture with an of OD 0.1 were spun down at 4000 rpm (3000
675 g) for 10 min and resuspended in 100 µl. This cell suspension was loaded into the feeding
676 channels and spun for 5 min at 3000 rpm using a spin coater (Polos SPIN150i, SPS) to
677 improve the loading of the cells into the growth channels.
678
679 The loaded chips were then mounted onto the microscope stage and connected to a syringe
680 pump (KD Scientific, USA) using tygon tubing (Cole Parmer, USA). A constant flow rate of
681 0.15 ml/h and a temperature of 37°C was maintained throughout the experiment. In all
682 experiments with P_{sigV}-YFP cells were first grown in SMM overnight for ~100 frames before
683 the media was switched to contain various levels of lysozyme (0.1, 0.5 or 1 µg/ml). Switching
684 was provided by disconnecting the tubing from media with 0 ug/ml lysozyme and connecting

the tubing to a new syringe with lysozyme stress. Subsequently, the tubing was flushed for 10 min at 10 ml/h.

All movies were analysed using a modified version of the Schnitzcells package (75) for MATLAB (Mathworks, USA) optimised for mother machine experiments.

Data availability

All data used in this paper, as well as all code for carrying out all analysis, and the generation of all figures, can be found here: https://gitlab.developers.cam.ac.uk/slcu/teamjl/loman_schwall_etal_2025. Repository README files and code comments direct users on its use. Julia's default package manager can be used to reproduce and install the exact package environment used. The repository contains the 6d behaviour maps, which is available for download and further investigation.

Acknowledgments

We thank Ozgur Akman and Diana Fusco for their extensive feedback on the modelling. We thank Romain Veltz for helping with the computation of the bifurcation diagrams. We are grateful for the high performance computing resources provided by the Cambridge Service for Data Driven Discovery. This research was made possible by the award of a European Research Council under the European Union's Seventh Framework Programme (FP/2007-2013)/ERC Grant Agreement 338060. The work in the Locke laboratory is further supported by a fellowship from the Gatsby Foundation (GAT3272/GLC), and a BBSRC grant award no. BB/V006088/1. Torkel Loman has received funding from the European Union's Horizon 2020 research and innovation programme under the Marie Skłodowska-Curie grant agreement No. 721456.

Bibliography

1. Xiong W, Ferrell JE. A positive-feedback-based bistable "memory module" that governs a cell fate decision. Nature. 2003 Nov 27;426(6965):460–5.
2. Umulis DM, Serpe M, O'Connor MB, Othmer HG. Robust, bistable patterning of the dorsal surface of the Drosophila embryo. Proc Natl Acad Sci USA. 2006 Aug 1;103(31):11613–8.
3. Goldbeter A. A minimal cascade model for the mitotic oscillator involving cyclin and cdc2 kinase. Proc Natl Acad Sci USA. 1991 Oct 15;88(20):9107–11.

4. Elowitz MB, Leibler S. A synthetic oscillatory network of transcriptional regulators. Nature. 2000 Jan 20;403(6767):335–8.

5. Hubaud A, Regev I, Mahadevan L, Pourquié O. Excitable Dynamics and Yap-Dependent Mechanical Cues Drive the Segmentation Clock. Cell. 2017 Oct 19;171(3):668-682.e11.

6. Süel GM, Garcia-Ojalvo J, Liberman LM, Elowitz MB. An excitable gene regulatory circuit induces transient cellular differentiation. Nature. 2006 Mar 23;440(7083):545–50.

7. Briat C, Gupta A, Khammash M. Antithetic integral feedback ensures robust perfect adaptation in noisy biomolecular networks. Cell Syst. 2016 Jan 27;2(1):15–26.

8. Park J, Dies M, Lin Y, Hormoz S, Smith-Unna SE, Quinodoz S, et al. Molecular Time Sharing through Dynamic Pulsing in Single Cells. Cell Syst. 2018 Feb 28;6(2):216-229.e15.

9. Arkin A, Ross J, McAdams HH. Stochastic kinetic analysis of developmental pathway bifurcation in phage lambda-infected Escherichia coli cells. Genetics. 1998 Aug;149(4):1633–48.

10. Gillespie DT. Stochastic simulation of chemical kinetics. Annu Rev Phys Chem. 2007;58:35–55.

11. Paranjpe DA, Sharma VK. Evolution of temporal order in living organisms. J Circadian Rhythms. 2005 May 4;3(1):7.

12. Lee B, Shin D, Gross SP, Cho K-H. Combined Positive and Negative Feedback Allows Modulation of Neuronal Oscillation Frequency during Sensory Processing. Cell Rep. 2018 Nov 6;25(6):1548-1560.e3.

13. Mugler A, Kittisopikul M, Hayden L, Liu J, Wiggins CH, Süel GM, et al. Noise Expands the Response Range of the Bacillus subtilis Competence Circuit. PLoS Comput Biol. 2016 Mar 22;12(3):e1004793.

14. Pomerening JR, Kim SY, Ferrell JE. Systems-level dissection of the cell-cycle oscillator: bypassing positive feedback produces damped oscillations. Cell. 2005 Aug 26;122(4):565–78.

15. Devany E, Zhang X, Park JY, Tian B, Kleiman FE. Positive and negative feedback loops in the p53 and mRNA 3’ processing pathways. Proc Natl Acad Sci USA. 2013 Feb 26;110(9):3351–6.

16. Afroz T, Beisel CL. Understanding and exploiting feedback in synthetic biology. Chem Eng Sci. 2013 Nov;103:79–90.

17. Shahrezaei V, Swain PS. The stochastic nature of biochemical networks. Curr Opin Biotechnol. 2008 Aug 9;19(4):369–74.

18. Briat C, Khammash M. Noise in biomolecular systems: modeling, analysis, and control implications. Annu Rev Control Robot Auton Syst. 2023 May 3;6(1).

19. Holehouse J, Cao Z, Grima R. Stochastic modeling of autoregulatory genetic feedback loops: A review and comparative study. Biophys J. 2020 Apr 7;118(7):1517–25.

20. Süel GM, Kulkarni RP, Dworkin J, Garcia-Ojalvo J, Elowitz MB. Tunability and noise dependence in differentiation dynamics. Science. 2007 Mar 23;315(5819):1716–9.

761 21. Barkai N, Leibler S. Circadian clocks limited by noise. Nature. 2000 Jan
762 20;403(6767):267–8.

763 22. Feklístov A, Sharon BD, Darst SA, Gross CA. Bacterial sigma factors: a historical,
764 structural, and genomic perspective. Annu Rev Microbiol. 2014 Jun 18;68:357–76.

765 23. Himmelreich R, Hilbert H, Plagens H, Pirkl E, Li BC, Herrmann R. Complete sequence
766 analysis of the genome of the bacterium Mycoplasma pneumoniae. Nucleic Acids Res.
767 1996 Nov 15;24(22):4420–49.

768 24. Gruber TM, Gross CA. Multiple sigma subunits and the partitioning of bacterial
769 transcription space. Annu Rev Microbiol. 2003;57:441–66.

770 25. Cook H, Ussery DW. Sigma factors in a thousand E. coli genomes. Environ Microbiol.
771 2013 Dec;15(12):3121–9.

772 26. Helmann JD. Anti-sigma factors. Curr Opin Microbiol. 1999 Apr;2(2):135–41.

773 27. Paget MS. Bacterial Sigma Factors and Anti-Sigma Factors: Structure, Function and
774 Distribution. Biomolecules. 2015 Jun 26;5(3):1245–65.

775 28. Davis MC, Kesthely CA, Franklin EA, MacLellan SR. The essential activities of the
776 bacterial sigma factor. Can J Microbiol. 2017 Feb;63(2):89–99.

777 29. Wang P, Robert L, Pelletier J, Dang WL, Taddei F, Wright A, et al. Robust growth of
778 Escherichia coli. Curr Biol. 2010 Jun 22;20(12):1099–103.

779 30. Schwall CP, Loman TE, Martins BMC, Cortijo S, Villava C, Kusmartsev V, et al.
780 Tunable phenotypic variability through an autoregulatory alternative sigma factor
781 circuit. Mol Syst Biol. 2021 Jul;17(7):e9832.

782 31. Locke JCW, Young JW, Fontes M, Hernández Jiménez MJ, Elowitz MB. Stochastic
783 pulse regulation in bacterial stress response. Science. 2011 Oct 21;334(6054):366–9.

784 32. Patange O, Schwall C, Jones M, Villava C, Griffith DA, Phillips A, et al. Escherichia
785 coli can survive stress by noisy growth modulation. Nat Commun. 2018 Dec
786 17;9(1):5333.

787 33. Young JW, Locke JCW, Elowitz MB. Rate of environmental change determines stress
788 response specificity. Proc Natl Acad Sci USA. 2013 Mar 5;110(10):4140–5.

789 34. Guariglia-Oropeza V, Helmann JD. Bacillus subtilis σ(V) confers lysozyme resistance
790 by activation of two cell wall modification pathways, peptidoglycan O-acetylation and
791 D-alanylation of teichoic acids. J Bacteriol. 2011 Nov;193(22):6223–32.

792 35. Ho TD, Hastie JL, Intile PJ, Ellermeier CD. The Bacillus subtilis extracytoplasmic
793 function σ factor σ(V) is induced by lysozyme and provides resistance to lysozyme. J
794 Bacteriol. 2011 Nov;193(22):6215–22.

795 36. Ho TD, Ellermeier CD. Extra cytoplasmic function σ factor activation. Curr Opin
796 Microbiol. 2012 Apr;15(2):182–8.

797 37. Hastie JL, Williams KB, Sepúlveda C, Houtman JC, Forest KT, Ellermeier CD.
798 Evidence of a bacterial receptor for lysozyme: binding of lysozyme to the anti-σ factor
799 RsiV controls activation of the ecf σ factor σV. PLoS Genet. 2014 Oct
800 2;10(10):e1004643.

801 38. Hastie JL, Williams KB, Bohr LL, Houtman JC, Gakhar L, Ellermeier CD. The Anti-

802 sigma Factor RsiV Is a Bacterial Receptor for Lysozyme: Co-crystal Structure
803 Determination and Demonstration That Binding of Lysozyme to RsiV Is Required for
804 σV Activation. PLoS Genet. 2016 Sep 7;12(9):e1006287.

805 39. Castro AN, Lewerke LT, Hastie JL, Ellermeier CD. Signal Peptidase Is Necessary and
806 Sufficient for Site 1 Cleavage of RsiV in Bacillus subtilis in Response to Lysozyme. J
807 Bacteriol. 2018 Jun 1;200(11):e00663-17.

808 40. Lewerke LT, Kies PJ, Müh U, Ellermeier CD. Bacterial sensing: A putative amphipathic
809 helix in RsiV is the switch for activating σV in response to lysozyme. PLoS Genet.
810 2018 Jul 18;14(7):e1007527.

811 41. Benson AK, Haldenwang WG. Characterization of a regulatory network that controls
812 sigma B expression in Bacillus subtilis. J Bacteriol. 1992 Feb;174(3):749–57.

813 42. Dufour A, Haldenwang WG. Interactions between a Bacillus subtilis anti-sigma factor
814 (RsbW) and its antagonist (RsbV). J Bacteriol. 1994 Apr;176(7):1813–20.

815 43. Alper S, Dufour A, Garsin DA, Duncan L, Losick R. Role of adenosine nucleotides in
816 the regulation of a stress-response transcription factor in Bacillus subtilis. J Mol Biol.
817 1996 Jul 12;260(2):165–77.

818 44. Wise AA, Price CW. Four additional genes in the sigB operon of Bacillus subtilis that
819 control activity of the general stress factor sigma B in response to environmental
820 signals. J Bacteriol. 1995 Jan;177(1):123–33.

821 45. Kalman S, Duncan ML, Thomas SM, Price CW. Similar organization of the sigB and
822 spoIIA operons encoding alternate sigma factors of Bacillus subtilis RNA polymerase.
823 J Bacteriol. 1990 Oct;172(10):5575–85.

824 46. Voelker U, Voelker A, Haldenwang WG. Reactivation of the Bacillus subtilis anti-sigma
825 B antagonist, RsbV, by stress- or starvation-induced phosphatase activities. J
826 Bacteriol. 1996 Sep;178(18):5456–63.

827 47. Chen C-C, Yudkin MD, Delumeau O. Phosphorylation and RsbX-dependent
828 dephosphorylation of RsbR in the RsbR-RsbS complex of Bacillus subtilis. J Bacteriol.
829 2004 Oct;186(20):6830–6.

830 48. Gillespie DT. The chemical Langevin equation. Journal of Chemical Physics.
831 2000;113(1):297–306.

832 49. Wilkinson DJ. Stochastic modelling for quantitative description of heterogeneous
833 biological systems. Nat Rev Genet. 2009 Feb;10(2):122–33.

834 50. Gillespie DT. A general method for numerically simulating the stochastic time evolution
835 of coupled chemical reactions. J Comput Phys. 1976 Dec;22(4):403–34.

836 51. Gillespie DT. Exact stochastic simulation of coupled chemical reactions. J Phys Chem.
837 1977 Dec;81(25):2340–61.

838 52. Metz J, Diekmann 0. Exact Finite Dimensional Representations of Models for
839 Physiologically Structured Populations.I: The Abstract Foundations of linear Chain
840 Trickery. Differential Equations with Applications in biology, Physics and Engineering,
841 Letcure Notes in Pure & Applied Mathematics. 1991. p. 269–89.

842 53. MacDonald N. Time lags in biological models. Berlin, Heidelberg: Springer Berlin
843 Heidelberg; 1978.

54. Ho TD, Ellermeier CD. Activation of the extracytoplasmic function σ factor σv by lysozyme. Mol Microbiol. 2019 Jul 9;112(2):410–9.

55. Rodriguez Ayala F, Bartolini M, Grau R. The Stress-Responsive Alternative Sigma Factor SigB of Bacillus subtilis and Its Relatives: An Old Friend With New Functions. Front Microbiol. 2020 Sep 15;11:1761.

56. Haldenwang WG, Losick R. A modified RNA polymerase transcribes a cloned gene under sporulation control in Bacillus subtilis. Nature. 1979 Nov 15;282(5736):256–60.

57. Hecker M, Pané-Farré J, Völker U. SigB-dependent general stress response in Bacillus subtilis and related gram-positive bacteria. Annu Rev Microbiol. 2007;61:215–36.

58. Brody MS, Stewart V, Price CW. Bypass suppression analysis maps the signalling pathway within a multidomain protein: the RsbP energy stress phosphatase 2C from Bacillus subtilis. Mol Microbiol. 2009 Jun;72(5):1221–34.

59. Loman TE, Locke JCW. The σB alternative sigma factor circuit modulates noise to generate different types of pulsing dynamics. PLoS Comput Biol. 2023 Aug 4;19(8):e1011265.

60. Yelleswarapu M, van der Linden AJ, van Sluijs B, Pieters PA, Dubuc E, de Greef TFA, et al. Sigma Factor-Mediated Tuning of Bacterial Cell-Free Synthetic Genetic Oscillators. ACS Synth Biol. 2018 Dec 21;7(12):2879–87.

61. Mancini R, Karki J. Voltage- and Current-Feedback Op Amp Comparison. Op amps for everyone. Elsevier; 2003. p. 113–21.

62. Jordan CF. Energy flow and feedback control in ecological and economic food systems. Ecological Economics. 2019 Feb;156:91–7.

63. van Breugel M, Bongers F, Norden N, Meave JA, Amissah L, Chanthorn W, et al. Feedback loops drive ecological succession: towards a unified conceptual framework. Biol Rev Camb Philos Soc. 2024 Jun;99(3):928–49.

64. Rhodius VA, Segall-Shapiro TH, Sharon BD, Ghodasara A, Orlova E, Tabakh H, et al. Design of orthogonal genetic switches based on a crosstalk map of σs, anti-σs, and promoters. Mol Syst Biol. 2013 Oct 29;9:702.

65. Bervoets I, Van Brempt M, Van Nerom K, Van Hove B, Maertens J, De Mey M, et al. A sigma factor toolbox for orthogonal gene expression in Escherichia coli. Nucleic Acids Res. 2018 Feb 28;46(4):2133–44.

66. Pinto D, Vecchione S, Wu H, Mauri M, Mascher T, Fritz G. Engineering orthogonal synthetic timer circuits based on extracytoplasmic function σ factors. Nucleic Acids Res. 2018 Aug 21;46(14):7450–64.

67. Loman TE, Ma Y, Ilin V, Gowda S, Korsbo N, Yewale N, et al. Catalyst: Fast and flexible modeling of reaction networks. PLoS Comput Biol. 2023 Oct 18;19(10):e1011530.

68. Rackauckas C, Nie Q. DifferentialEquations.jl – A Performant and Feature-Rich Ecosystem for Solving Differential Equations in Julia. J Open Res Softw. 2017 May 25;5.

69. Rackauckas C, Nie Q. Adaptive methods for stochastic differential equations via

886 natural embeddings and rejection sampling with memory. Discrete Continuous Dyn
887 Syst Ser B. 2017;22(7):2731–61.

888 70. Zagatti G, Isaacson S, Rackauckas C, Ilin V, Ng S-K, Bressan S. Extending
889 JumpProcesses.jl for fast point process simulation with time-varying intensities. JCON.
890 2024 Apr 23;6(58):133.

891 71. Veltz R. BifurcationKit.jl. 2020 Jul;

892 72. Spizizen J. Transformation of biochemically deficient strains of bacillus subtilis by
893 deoxyribonucleate. Proc Natl Acad Sci USA. 1958 Oct 15;44(10):1072–8.

894 73. Eldar A, Chary VK, Xenopoulos P, Fontes ME, Losón OC, Dworkin J, et al. Partial
895 penetrance facilitates developmental evolution in bacteria. Nature. 2009 Jul
896 23;460(7254):510–4.

897 74. Norman TM, Lord ND, Paulsson J, Losick R. Memory and modularity in cell-fate
898 decision making. Nature. 2013 Nov 28;503(7477):481–6.

899 75. Young JW, Locke JCW, Altinok A, Rosenfeld N, Bacarian T, Swain PS, et al.
900 Measuring single-cell gene expression dynamics in bacteria using fluorescence time-
901 lapse microscopy. Nat Protoc. 2011 Dec 15;7(1):80–8.